Strength-hardness relationship for AlSi10Mg alloy produced by laser powder bed fusion: An experimental study

A. Serjouei [a],[*], T. Libura [b], A. Brodecki [b], J. Radziejewska [b], P. Broniszewska [b], P. Pawłowski [b], T. Szymczak [c], M. Bodaghi [a], Z.L. Kowalewski [b]

[a] Department of Engineering, School of Science and Technology, Nottingham Trent University, Nottingham, NG11 8NS, United Kingdom
[b] Institute of Fundamental Technological Research of the Polish Academy of Sciences, 02-106, Warsaw, Poland
[c] Motor Transport Institute, Jagiellonska 80, 03-301, Warsaw, Poland

ARTICLE INFO

ABSTRACT

In this work, significant strength and ductility variations are reported for AlSi10Mg parts fabricated at different orientations using laser powder bed fusion (LPBF). Hardness and surface roughness of the specimens at different orientations were measured. Tensile testing together with digital image correlation technique were conducted on the specimens. XY specimens showed the highest yield stress and ultimate tensile strength while XZ specimens showed the highest ductility. Hardness measurements for different specimens were in accordance with the tensile test results, following the same order as the UTS values, XY specimens being the highest and XY-45° (out-of-plane) specimens being the lowest. Fractography of the broken surfaces of the specimens under tensile testing revealed the microstructural features and various defects in the tensile fracture. The anisotropy in mechanical properties is attributed to the microstructural anisotropy as well as presence of various types of defects induced by the AM process, which affects the deformation and failure mechanism of the parts. Linear relationships between experimental Vickers hardness versus yield stress and UTS measurements were developed. In case of material selection for different applications, these relationships can be used as a simple tool for converting hardness and yield stress (or UTS) values to each other. An equivalent strain-hardness relationship was also proposed which can be used for health monitoring of parts subject to tensile loading.

1. Introduction

Additive manufacturing (AM) with favourable time- and cost-effective benefits and great net-shape production capability has claimed its position at the forefront of manufacturing technologies in various industries such as space, aerospace, biomedical and armour [1]. With respect to the technical features, AM enables producing objects at various sizes and shapes, e. g., in manufacturing dental implants [2]. It should also be noted that new computational approaches should be considered for the analysis of behaviour of AM materials under different loading conditions, such as studying the fracture toughness of parts under the conditions of geometrically defined cracks in a three-dimensional solid body [3–5].

Among others, AM aluminium alloys with high strength to weight ratio, large thermal conductivity and reflectivity have attracted specific attention of aircraft and automotive industries [6,7]. AlSi10Mg is the most extensively studied among AM aluminium alloys [8–11]. While AM

technologies provide exceptional features such as design freedom, material waste reduction, etc., presence of unfavourable features such as internal defects, surface roughness, residual stress, etc. has affected the microstructure and structural integrity of the AM parts. The influencing parameters affecting these features in LPBF process are related to four main controlling factors [12]: (a) laser such as laser power, pulse frequency, (b) powder such as particle size, shape and distribution, (c) scan such as scan speed and scan spacing and (d) temperature such as powder bed temperature.

Numerous studies focused on the influence of the LPBF process parameters as well as improving methods such as heat treatment or surface treatment such as machining on microstructure and mechanical properties of AlSi10Mg parts fabricated by LPBF process. Pola et al. [13] showed that sand-blasting surface treatment improved the surface roughness and fatigue strength of AlSi10Mg specimens produced by direct metal laser sintering (DMLS). Thijs et al. [14] presented LPBF production of very fine-microstructure AlSi10Mg parts with high hardness value of 127 ± 3 HV0.5. They discussed that different scanning

Nomenclature and abbreviations

AM	Additive Manufacturing
BD	Building Direction
DED	Directed Energy Deposition
DIC	Digital Image Correlation
DMLS	Direct Metal Laser Sintering
E	Young's Modulus
FEA	Finite Element Analysis
HAZ	Heat Affected Zone
HF	Hydrofluoric acid
H_V	Vickers hardness
LPBF	Laser Powder Bed Fusion
R_a	Mean roughness value
R_z	Maximum height of roughness profile
STDEV	Standard Deviation
S	Mean spacing of picks
S_m	Mean spacing of profiles irregularities
SEM	Scanning Electron Microscopy
XY	Parallel to build plat in 0°
XY-45° (in-plane)	Parallel to build plat in 45°
XY-45° (out-of-plane)	Angled out-of-plane with 45° to build plate
YX	Parallel to build plat in 90°
ZX	Angled out-of-plane with 90° to build plate
Yb	Ytterbium
ε_e	Huber-von Mises-Hencky strain
ε_f	Strain at fracture
ε_x Strain component in x directionε_y	Strain component in x directionε_y Strain component in y direction
v Effective Poisson's ratioσ_Y	Effective Poisson's ratioσ_Y Yield Stress
σ_U, UTS	Ultimate Tensile Strength

strategies can be used to control the anisotropy of the parts. Read et al. [15] showed superior strength, elongation and creep properties of LPBF AlSi10Mg parts fabricated using a Concept Laser M2 system compared to the cast counterpart alloy. Brandl et al. [10] showed that synergy of 300 °C powder-bed heating and a specific peak-hardening (combination of solution heat treatment, water quenching and artificial aging) improved the fatigue strength of LPBF-printed AlSi10Mg parts and reduced the difference between cyclic life of specimens printed at different orientations. Li et al. [16] showed that solution heat treatment and artificial aging have significant influence on the microstructure and mechanical properties of AlSi10Mg specimens fabricated by LPBF. They showed that solution treatment at 550 °C for 2 h decreases the ultimate tensile strength (UTS) of as-built specimens from 434.25 ± 10.7 MPa to 168.11 ± 2.4 MPa and increases the fracture strain considerably from 5.3 ± 0.22% to 23.7 ± 0.84%. Manfredi et al. [17,18] studied the effects of annealing (T2), T4 (solution heat treated at the temperature of 530 °C for 5 h, and then, quenched in water) and T6 (solution heat treated at the temperature of 530 °C for 5 h, then quenched in water and artificially aged at 160 °C for 12 h) heat treatments on the UTS, ductility and hardness of AlSi10Mg specimens fabricated by DMLS. It was observed that tensile properties of AlSi10Mg specimens were lowered by all the heat treatment conditions as compared to the as-built condition.

It has been shown that building orientation is influential on the microstructure, anisotropy and producing different defects in the LPBF parts [19–21]. However, limited works have explored the effect of building orientation on the hardness of AlSi10Mg specimens. Read et al. [15] reported not major influence of building direction (BD) on tensile properties, and only ~10% higher UTS for LPBF-printed AlSi10Mg horizontal specimens was observed in comparison to that of vertical ones. Mfusi et al. [22] studied the microstructure and mechanical properties of AlSi10Mg printed using a Solutions M280 LPBF system in the XY, 45° and Z orientations. They found that the specimens in Z and 45° orientations show the highest UTS and elongation, respectively, while the XY specimens contain the lowest porosity, ductility and UTS. Kempen et al. [23] observed that AlSi10Mg parts fabricated using a Concept Laser M1 LPBF system exhibited comparable or higher Vickers hardness compared to the high pressure die cast AlSi10Mg parts depending on the aged or as-cast condition of the cast parts, respectively. They also showed that XY specimens have almost the same UTS, and higher ductility compared to the Z specimens. It is necessary to find out the effect of various building orientations both in XY and Z plane on the mechanical properties of AM AlSi10Mg parts.

Resistance of a material against local plastic deformation is measured by hardness. Attributes of material such as microstructure [24] and strain-hardening [25] have direct influence on the hardness, and this makes hardness a non-intrinsic material property. Empirical relationships between hardness/microhardness of metals and a measure of their strength such as UTS or YS have been developed. For example, the following general relationship has been proposed between Vickers hardness, H_V, and yield stress, σ_Y, of metals exhibiting minimal strain hardening [26]:

$$\sigma_Y = \frac{H_V}{0.927C} \tag{1}$$

Tabor [26] experimentally proved that the constant C for fully work-hardened mild steel, annealed copper and tellurium lead is 2.8, 2.8 and 2.9, respectively. Based on this, Tabor [26] considered $C \approx 3$. As an example using Eq. (1), if $C = 2.9$, the slope of H_V (in MPa) versus σ_y (in MPa) will be 0.372 going through the origin. However, for materials with strain-hardening behaviour corresponding to steels, magnesium, aluminium and copper alloys the strength-hardness relationship can be better described by Ref. [27]:

$$\sigma_y = AH_V + B \tag{2}$$

where A and B are the fitting constants in this linear relationship. Equations such as Eq. (2) have been used to provide insight on the nature of relationship between strength and hardness over an examined range, e. g., in Refs. [28–30]. It may be expected that the constant B in Eq. (2) to be zero since a material with zero hardness should also have zero strength. However, a standard error is normally associated with the constant B in such fitting equations which justifies the non-zero value of B [31].

The relationship between hardness and strength for AM materials is not widely recognized. Keist and Palmer [32] showed, that there is a strong linear correlation, similar to Eq. (2), between the hardness and yield stress or UTS of additively manufactured (directed energy deposition (DED), laser-based DED, and laser-based powder bed fusion (LPBF)) Ti–6Al–4V alloy which often experiences a strong strain hardening. Cerri and Ghio [33] stated, that Eq. (2) is also suitable for adequate description of the strength-hardness relationship for AlSi10Mg alloy produced by LPBF and post-processed under different thermal treatment conditions. Further research needs confirmation of validity of strength-hardness relationships such as Eq. (2) for different AM materials fabricated using different process conditions including various building orientations. The relationship between hardness and plastic strain has been also studied for ductile metals. It was observed that a stretching of metals make them harder up to the point of UTS after which a further loading leads to the local necking and/or fracture [34]. Some theoretical approaches or finite element analysis (FEA) results devoted to Vickers hardness increase due to plastic deformation have been reported by many research centres, e.g. Refs. [35–38].

This research is conducted to address the of above limitations in lack

of experimental works on the effect of building orientation on the hardness and validity of strength-hardness relationships for AM materials. In this work, the effect of various building orientations on the mechanical properties of AM AlSi10Mg parts is studied. Microstructural analysis was performed to observe different types of defects. Hardness and surface roughness of the specimens were measured along different orientations. Equations for Vickers hardness-strength dependency of AlSi10Mg alloy fabricated along different orientations by LPBF are proposed based on the experimental data. In addition, the relationship between equivalent strain and post tensile hardness values were studied for AM specimens. Tensile test supported by digital image correlation (DIC) technique were conducted. Fractography of the broken specimens under tensile loading enabled description of failure mechanism due to presence of microstructural features such as defects.

2. Materials and testing methods

2.1. Details of specimens' fabrication and procedure of their quality check

An EOS M280 DMLS system of a powder bed fusion, metal 3D printer was used to manufacture specimens. The main unit was equipped with a Ytterbium (Yb) fibre laser with a wavelength of 1060–1100 nm and a maximum power of 400 W. The working volume of the machine was 250 mm × 250 mm × 320 mm, and the process was carried out in an argon gas atmosphere, with oxygen content in the building chamber below 1000 ppm (0.1 vol percentage). The aluminium base plate was kept at a constant temperature of 35 °C. The general laser scanning strategy in case of the selected 30 μm layer thickness consisted of two subsequent steps: the exposition of the inner area (green area) and the external contour (red line) of the part, Fig. 1(a). The inner area was filled by the parallel laser lines (green lines) with a distance of 190 μm (D_b), creating hatched pattern. In order to avoid an excessive heat generation in the long lines, the hatched area was divided into 7 mm wide stripes (D_s) (blue lines in Fig. 1(a)) with 0.02 mm overlaps. The adopted scanning velocity was equal to 1300 mm/s and the laser power was 370 W. The hatched pattern was rotated by 67° angle with respect to the consecutive layers, providing a higher level of homogeneity. The general view of patterns for selected cross-sections is depicted in Fig. 1(b). The

exposure parameters, i.e., laser beam velocity and power for the last three bottom and top surface layers (so-called up-skin and down-skin) were reduced by approximately 20% and 10%, respectively. The outer contour was double exposed to the laser radiation with 0.02 mm offset distance, a scanning velocity of 900 mm/s and power of 85 W. The outer contour exposition provided surface quality and a small number of defects in the transition zone to inline hatching. In turn, Fig. 1(c) shows dimensions of the plane specimen which are in agreement with ASTM E8/E8M − 09 [39].

The AlSi10Mg powder with average particle size within the range of 15–45 μm was used for 3D printing. The chemical composition of the AlSi10Mg powder applied for printing is listed in Table 1. Fig. 2 shows the morphology of the powder captured by scanning electron microscopy (SEM) using a Joel JSM-6480 series system. Although most of the particles had a spherical shape, there were satellites attached to them or porosities observed inside them. The specimens were printed in several processes alongside other parts designed for different purposes. A layout of the base plate for the selected printing process is presented in Fig. 3 (a).

Fig. 3(b) presents six orientations of the specimens: three parallel to the build plate plane in 0°, 45° and 90°, representing directions denoted as XY, XY-45° (in-plane) and YX, respectively, two representing out-of-plane directions included by 45° and 90° with respect to the build plate XY-45° (out-of-plane) and ZX, respectively, and one printed perpendicularly with regard to specimens XY, denoted as XZ. The bottom part of all specimens was supported by a regular, rectangular lattice with a spacing of 0.6 mm × 0.6 mm. The inclined specimens (XY-45° (out-of-plane)) were self-supported and did not require an additional support structure along their main axis. All specimens were subjected to stress relief annealing for 2 h at 300 °C.

3D printing precision of specimens was checked on a Form Talysurf system using UltraContur version 30303 of 1 μm accuracy. Five specimens were printed in each direction for the purpose of repeatability check of the results. Five specimen dimensions that were crucial from experimental point of view (see Fig. 4) were examined. Their average values together with standard deviation are reported in Table 2. A reasonably good agreement between required and obtained specimen dimensions was achieved. The high surface roughness and high
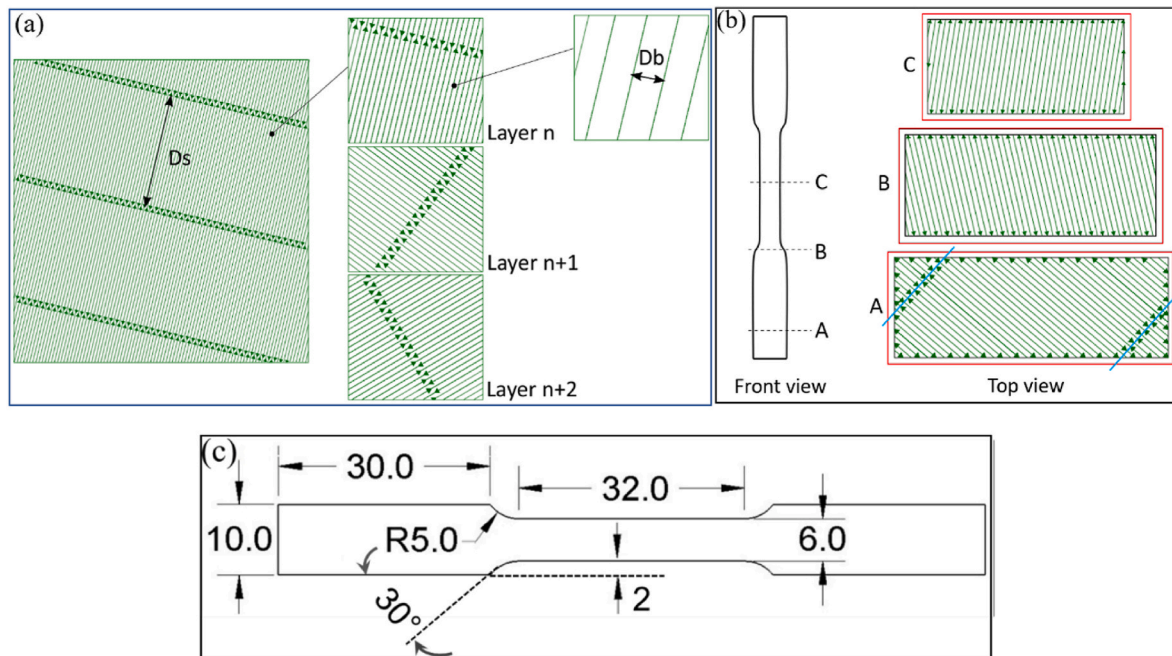

Fig. 1. Details of the process for specimen fabrication: (a) schematic of the exposure strategy; (b) exposure patterns for selected cross-sections of the specimen; (c) engineering drawing of the specimen (in agreement with ASTM E8/E8M − 09 [39], dimensions are in mm); the nominal thickness of the specimens is 4 mm.

Table 1

Chemical composition (mass %) of the AlSi10Mg powder.

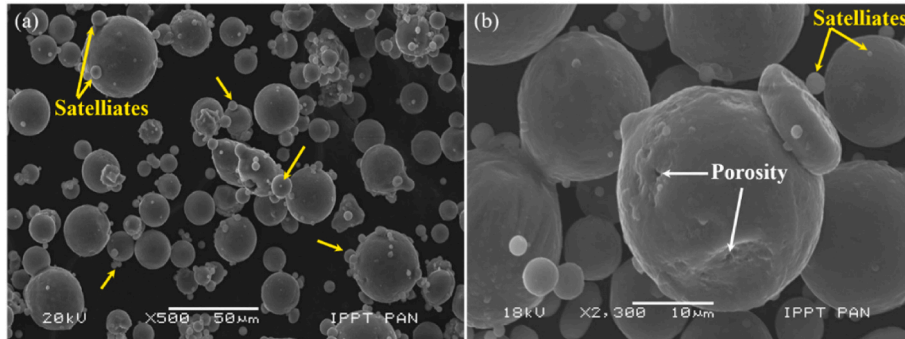| Cu	Si	Mn	Fe	Mg	Ni	Zn	Pb	Sn	Ti
<0.05	9–11	<0.45	<0.55	0.2–0.45	<0.05	<0.1	<0.05	<0.05	<0.15

Fig. 2. SEM images of the AlSi10Mg powder used for 3D printing.
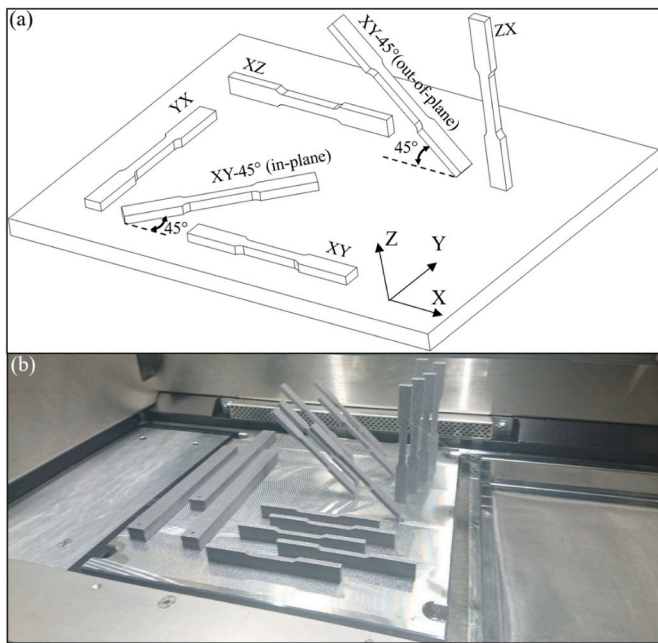

Fig. 3. Configuration of specimens showing their orientations considered: (a) schematic visualization; (b) general view of the AM specimens.

concentration of unmelted powder particles led to the large scatter of the results, especially in the case of radii. The highest accuracy was found for the XZ specimen.

2.2. Testing techniques for material characterisation

In this research several methods were applied to determine a range of mechanical properties of AM materials in question. The experimental program comprised techniques for either macroscopic or microscopic characterisation of the material. Among macroscopic techniques one can indicate: hardness measurements, surface roughness inspection and tensile tests. In the case of microscopic investigations, an identification of the material structure was captured in the as-received state and after specimen fracture.

The Vickers hardness measurement (under force equal to 5 kgf) were performed using a Duramin-500 universal hardness tester on the cross-sections perpendicular to the longer axis of specimens. Hardness was analysed either in the gauge length of specimens or in the gripping part. Tests were carried out according to the ISO 6507-1 standard [40]. Five imprints were made on each specimen.

Table 2

Nominal and measured dimensions (see Fig. 4) of the printed specimens.

| Dimensions/Orientations	R_1 (mm)	R_2 (mm)	φ_1 (°)	φ_2 (°)	C_1 (mm)
Nominal values	5.00	5.00	150.00	150.00	2.00
XY	5.31 ± 0.07	5.12 ± 0.17	149.48 ± 0.87	150.07 ± 0.05	1.98 ± 0.00
XY-45° (in-plane)	4.87 ± 0.02	4.87 ± 0.01	148.85 ± 2.50	152.16 ± 0.34	2.14 ± 0.00
YX	4.92 ± 0.24	5.14 ± 0.04	148.42 ± 1.16	151.76 ± 1.06	1.87 ± 0.00
ZX	5.01 ± 0.08	5.33 ± 0.36	149.91 ± 0.00	151.31 ± 0.03	1.88 ± 0.03
XY-45° (out-of-plane)	4.60 ± 0.01	5.12 ± 0.30	150.35 ± 0.40	149.65 ± 0.40	2.07 ± 0.05
XZ	4.90 ± 0.03	5.05 ± 0.01	149.83 ± 0.03	149.04 ± 0.83	2.005 ± 0.00
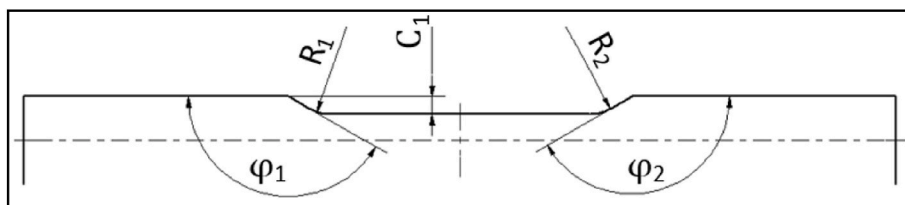
Fig. 4. Specimen dimensions considered for the validation of the 3D printing precision.

A stylus profilometer Form Talysurf system (Taylor Hobson Precision, UK, Series 2) of ± 0.5 mm measurement range, 40 mm maximum gauge length, 0.6 nm resolution and 2 μm tip radius, was used for the surface roughness measurement of all specimens. The surface roughness was measured along the longer axis of each specimen at five positions in order to check their repeatability. Four parameters were determined, namely mean roughness R_a, maximum height of roughness profile, R_z, mean spacing of picks, S, and mean spacing of profiles irregularities S_m. In addition, the mean standard deviation (STDEV) was calculated for each measurement. Tensile tests were performed on flat specimens, Fig. 1(c), for each printing orientations taken into account. Specimens were directly printed to the final-shape according to the ASTM Standard E8-09 [39]. MTS 810 testing machine of a maximum force equal to ± 250 kN and a maximum displacement range of ± 80 mm was applied in all tensile tests. Each test was performed at room temperature in accordance to the EN-ISO-6892-1 standard [41]. A displacement control mode with strain rate of 0.001 s^{-1} was applied in all tests. Three specimens of each building direction were tested. The axial strain was determined using an extensometer, MTS 634.31F-24, of the gauge length equal to 35 mm, while the transverse strain was measured using DIC.

The Aramis 12 M DIC system (Titanar B 75 lenses with a focal length of 75 mm) enabled to capture images at the resolution of 4096 × 3000 pixels and measurement zone represented by a rectangular field of dimensions within the range from 25 mm × 15 mm up to 1500 mm × 700 mm. The device was calibrated for the volume range of 190 mm × 135 mm × 120 mm, using the CP40-170-42201 calibration plate. Recording frequency for image capturing was constant and equal to 2 Hz. Strain components along the length and width of the specimens were determined directly by the DIC system, based on measurement frames covering area of 180 mm × 130 mm (4240 × 2824 pixels) as shown in Fig. 5(a). Fig. 5(b) shows the measuring points X_1 to X_5 and Y_1 to Y_5 were distinguished along the transverse direction on the specimen, in order to define strain components, ε_x and ε_y, within the area of interest shown in Fig. 5(a).

Microstructures of the specimens were examined on the cross-section perpendicular to the longer axis of each specimen using a VK-X100 confocal laser microscope. The process of metallographic specimens' preparation contained the following steps: firstly, specimens were cut in their gripping part; they were then subjected to the grinding and consecutive polishing using a diamond suspension of 9, 3 and 1 μm grades; and finally, specimens were etched using a 1% Hydrofluoric acid (HF) in period of 5 s. Fractured regions were inspected under different magnifications, using a Joel JSM-6480 series SEM system, in order to identify some structural effects or possible defects.

Poisson's ratio was calculated based on DIC measurements along axial and transverse directions for all specimens. It was subsequently used to calculate the values of equivalent strain according to Eq. (5).
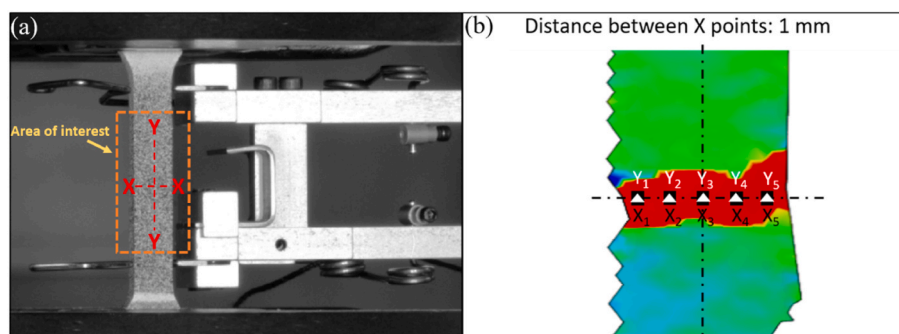
3. Results and discussion

3.1. Microstructural analysis

Fig. 6 shows optical microscopy images of three specimens, XZ, XY and XY-45° (out-of-plane). Fig. 6(a) and (b) shows microstructure near the one of corners of one of the XZ specimens. It can be observed, in Fig. 6(b) and (f) that melt pools share two boundaries with surroundings: one with the adjacent melt pools, track-track boundary, and the other with the bottom layer, layer-layer boundary. Distance between tracks is about 200 μm, which corresponds to the distance between each scan line (190 μm). The size of melt pools are different and the biggest is for the track on the specimen's corner. Single small pores are present located mainly on the boundaries of layers. A fine microstructure with cellular-dendritic structure is observed inside of the tracks (see Fig. 6 (b)). Toward the melt pool boundaries and overlap of adjacent melt pools, the grains become coarser due to long exposure to high temperature.

The layer-by-layer AM process entails a unique thermal history with rapid heat conduction from the melt pools towards dispersed cool surroundings which results in rapid solidifications. The microstructural anisotropy including different grain size and crystallographic orientations is mainly generated during this thermal process applied at different locations of the material. The microstructural anisotropy together with the presence of various types of defects generated during AM process are the sources of anisotropy in mechanical behaviour of the parts which affect their deformation and failure mechanisms.

As remelting and solidification occur, pores such as those observed in Fig. 6(c) and (e) are generated on the edges of the melt pools, and therefore, these sites become the preferential places of fracture due to pores opening and crack initiation. On the boundary of the track-track, a very fine dendritic microstructure and heat affected zone (HAZ) can be observed. Layer-layer boundary is narrow with fine grains. The microstructure of XY specimen is similar to that of XZ one. Cracks are located near the surface between near-to-edge track boundary (see Fig. 6(c)) and on the track-track boundaries. They initiate from the surface where oxide inclusions are observed. For XY-45° (out-of-plane) specimen, more and bigger pores were detected in comparison to those for XY specimens obtained, as shown in Fig. 6(e). These pores are located inside the melt pool tracks. Single cracks can be indicated near the surface of track-track border on the top layer and on the side surface as well.

3.2. Results of mechanical tests

Before execution of the main part of experimental program all specimens were subjected to the surface roughness measurement. The results are summarized in Table 3.

The amplitude parameters R_a, and R_z show that specimens representing XY-45° (in-plane) and XY directions exhibited the largest surface

Fig. 5. (a) DIC setup used to observe gauge zone during tensile test; (b) a digital profile of the middle section of gauge zone with the points representing places of strain analysis.
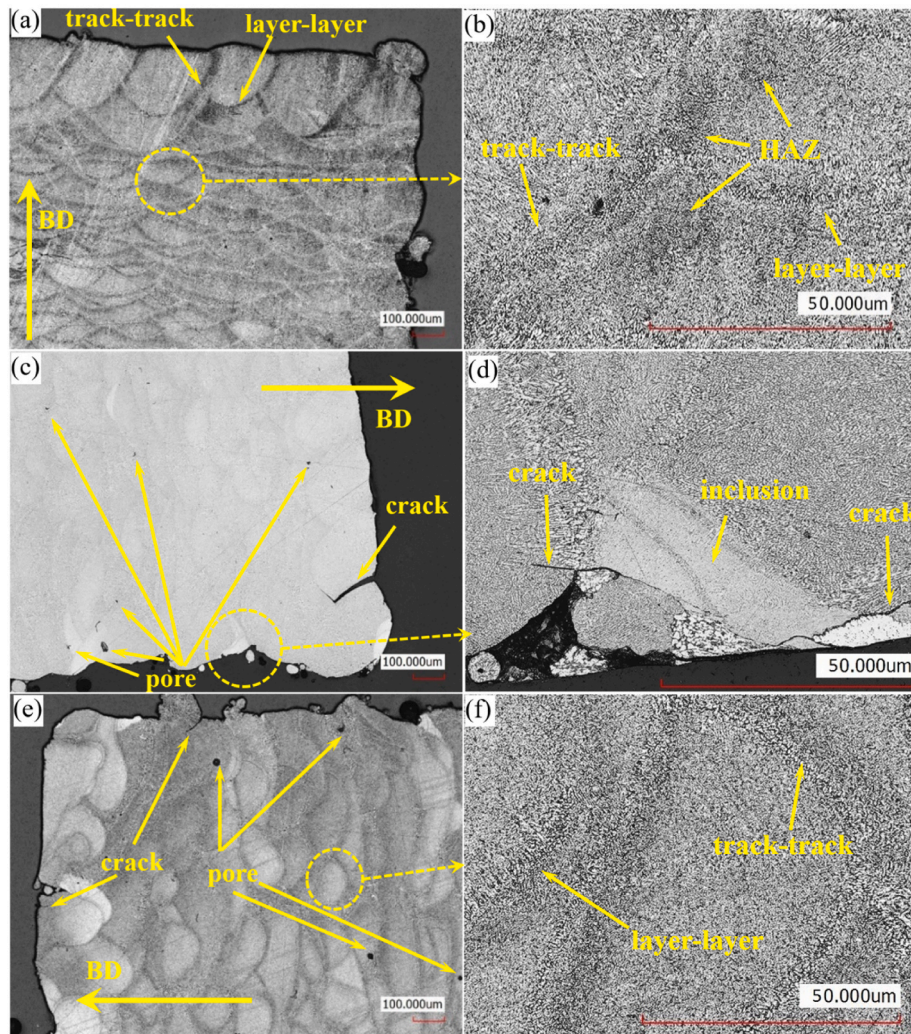
Fig. 6. Optical microscopy images of the specimens: (a) XZ, (c) XY and (e) XY-45° (out-of-plane); (b), (d) and (f) are the magnified views of specific sections in (a), (c) and (e), respectively. BD (building direction) is shown in each image.

Table 3
Results of the surface roughness measurements for the specimens printed in different orientations.

Building direction	R_a (μm)		R_z (μm)		S (μm)		S_m (μm)	
	Value	STDEV	Value	STDEV	Value	STDEV	Value	STDEV
XY	22.55	0.48	149.19	2.97	258	10	542	29
XY-45° (in-plane)	23.87	0.63	157.78	3.80	262	6	527	42
YX	19.29	0.56	132.43	6.72	246	10	585	50
XZ	16.78	0.96	123.44	7.31	246	7	521	77
XY-45° (out-of-plane)	22.25	1.41	151.81	7.60	267	26	552	40
ZX	21.97	0.65	137.53	6.51	239	11	519	36

roughness. Contrary to that, the specimens oriented as XZ and YX demonstrated the lowest surface roughness heights. In case of the mean spacing of picks, S, and mean spacing of profiles irregularities S_m, the lowest values for the ZX and XZ specimens were observed. The variations of the values of S or S_m parameters for the specimens printed in different directions are small and does not exceed over a dozen percent. The S_m parameters can be correlated with size of the melt pool on the edges of the specimens, that is more than two times larger than inside the specimen. This effect is shown in Fig. 6(a). To check whether the order of the roughness results correspond somehow to the selected mechanical parameters determined from the standard tensile tests a range of such experiments were carried out at room temperature. Tensile stress-strain curves for the flat specimens are shown in Fig. 7, while the

selected parameters determined on their basis are presented in Fig. 8. Values of the yield stress (σ_Y), ultimate tensile strength (UTS) and strain at fracture, ε_f, are summarized in Table 4. Significant anisotropy is observed for this material which should be taken into account in computational modelling where constitutive equations are developed for AlSi10Mg manufactured using LPBF process. The experimental results reported here agree well with data presented in the literature for LPBF AlSi10Mg alloy parts, e. g., in Refs. [42,43]. The mechanical properties presented here along with dynamic [44,45], compressive [46, 47], fatigue [48,49], fracture toughness [50,51], creep resistance [15], impact [46,52], wear [53,54] and flexural bending [55,56] studied behaviour of AlSi10Mg show great potential of this alloy for applications in aerospace, automotive, and biomedical industry.
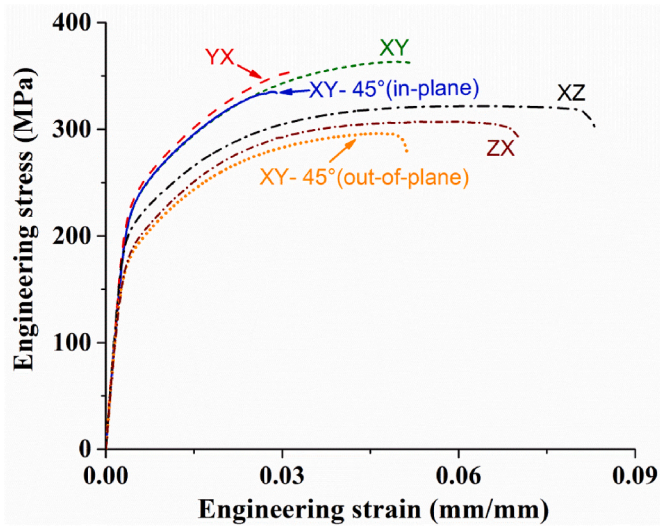
Fig. 7. Stress-strain tensile characteristics at room temperature for specimens printed along different directions.

The tensile properties of AlSi10Mg from EOS [57] are also included as a reference to the experimental data of this research. The XY specimens exhibited slightly higher Young's modulus, E, than that determined for ZX specimens. The XY specimens showed considerably higher yield stress, σ_Y, and UTS (σ_U) in comparison to ZX ones. The strain at fracture (ductility) can be ordered from the highest to lowest corresponding to the specimen orientations as: XZ > ZX > XY ≈ XY-45° (out-of-plane) > YX > XY-45° (in-plane). Similarly, the UTS values gave the following order: XY > YX > XY-45° (in-plane) > XZ > ZX > XY-45° (out-of-plane).

Applying DIC system, allowed determining the value of the strain components: ε_x and ε_y in the area of interest, just before fracture. Fig. 9

shows their values measured just before the fracture, in transverse and axial directions, ε_x and ε_y, respectively, at different X and Y points presented in Fig. 5(b)). It can be seen in Fig. 9(b) that the values of transverse strain, ε_x, are not uniform. They are most similar in points X_2 for all analysed specimens Therefore, all post tensile test hardness measurements were carried out in the location indicated by a vertical dashed line at points X_2 and Y_2.

The strain fields registered by DIC system, just before and after the fracture, for specimens printed in different directions are illustrated in Fig. 10. The fracture locations are marked with red arrows. It is clearly visible that the largest amount of strain can be observed in fracture area before and after the fracture. Then, the strain is released in the areas

Table 4
Mechanical properties of the printed and stress-relieved AlSi10Mg specimens determined from the standard tensile tests.

Specimen type/ direction	E (GPa)	σ_Y (MPa)	σ_U (UTS) (MPa)	ε_f (%)
XY	67.9 ± 4.5	243.6 ± 7.2	366.6 ± 4.6	4.7 ± 0.3
XY-45° (in-plane)	68.8 ± 3.4	238.3 ± 7.0	332.6 ± 4.9	2.8 ± 0.0
YX	68.8 ± 3.7	244.5 ± 2.1	349 ± 7.0	3 ± 0.2
XZ	67.9 ± 0.9	209.3 ± 2.9	327.8 ± 8.6	7.2 ± 1.1
XY-45° (out-of-plane)	66.1 ± 1.2	198.3 ± 3.6	295.8 ± 7.1	4.6 ± 0.5
ZX	65.8 ± 1.1	197.7 ± 3.5	306.1 ± 1.4	5.9 ± 1.5
EOS 0°, as-built	75 ± 10	270 ± 10	460 ± 20	9 ± 2
EOS 0°, stress-relieved[a]	70 ± 10	230 ± 15	345 ± 10	12 ± 2
EOS 90°, as-built	70 ± 10	240 ± 10	460 ± 20	6 ± 2
EOS 90°, stress-relieved[a]	60 ± 10	230 ± 15	350 ± 10	11 ± 2

[a] Annealed for 2 h at 300 °C according to EOS data extracted from Ref. [57].
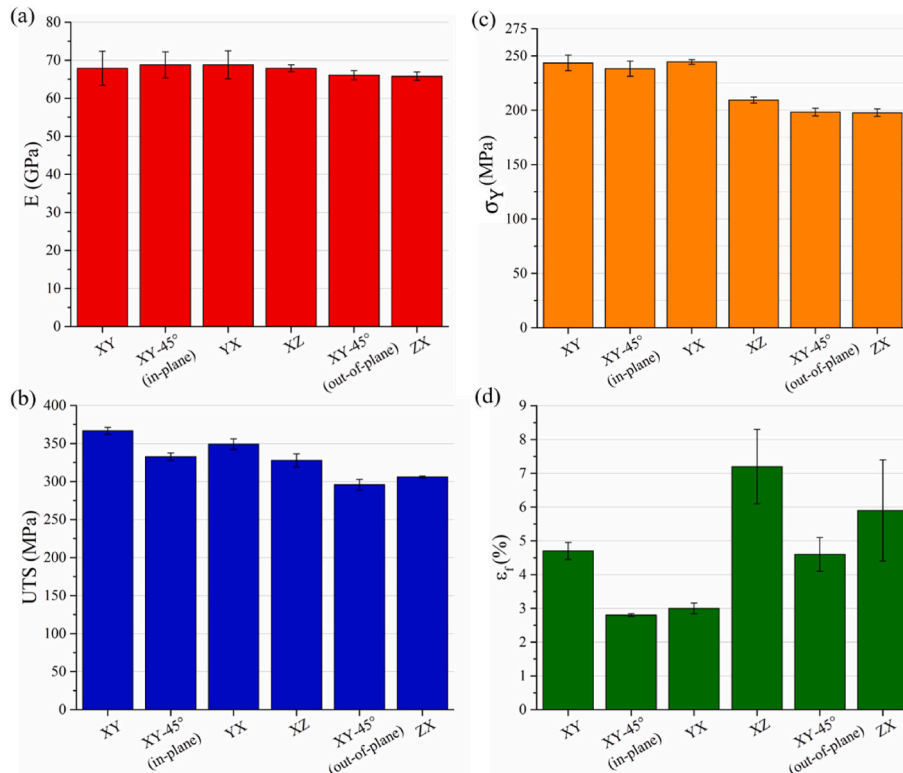

Fig. 8. Comparison of mechanical properties for the printed and stress-relieved AlSi10Mg specimens.
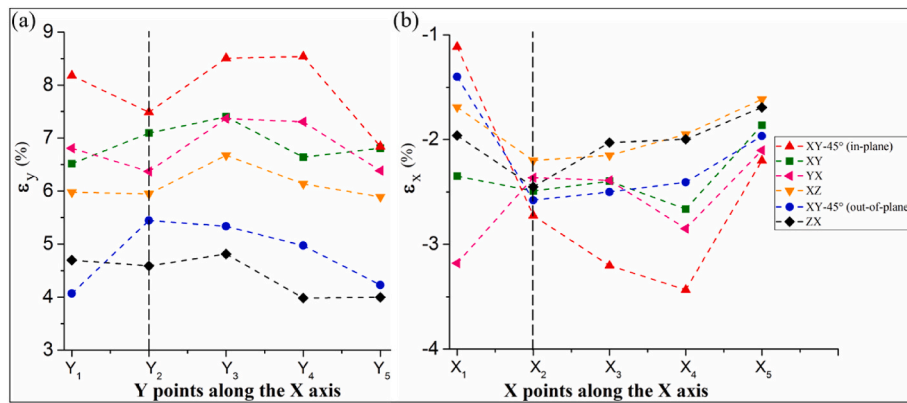
Fig. 9. Variations of ε_y and ε_x strain components at (a) Y points and (b) X points shown in Fig. 5(b).

located far from the fracture point. Most of analysed fractured surfaces are not perpendicular to the loading direction which is typical for the 3D printed specimens. Fractured surfaces are not normally flat and not vertical to the loading direction and even for the specimens in the same batch printed in the same direction, the orientation of the fracture surface might be different. This is due to stochastic nature of the defects' size and spatial distribution existing in the AM materials which makes the specimens' fracture surface and orientation unpredictable [58,59]. The Poisson's ratios based on the DIC system observation for all

specimens concerned are listed in Table 5. Their values are in the range 0.305–0.345 and the average value is 0.321.

The hardness measurements were carried out on two different sets of specimens: To find the hardness values of the as-built specimens, some of the printed specimens were cut in their gauge area and their hardness was measured in that area; no tensile tests were performed on these specimens. After performing tensile tests on another set of specimens, we first performed fractography on their fractured surfaces and then carried out post tensile test hardness measurement in the gauge area
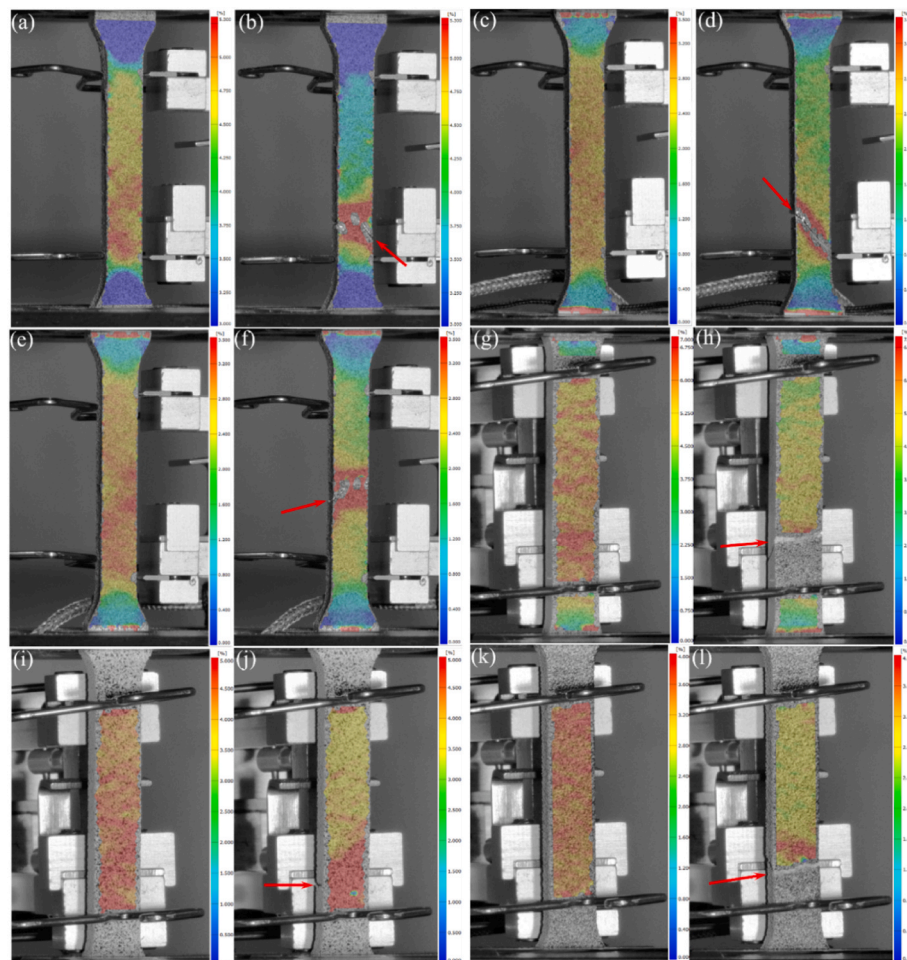

Fig. 10. DIC strain fields from uniaxial tensile tests just before and after the fracture, respectively, for different specimens: (a) and (b) XY, (c) and (d) XY-45° (in-plane), (e) and (f) YX, (g) and (h) XZ, (i) and (j) XY-45° (out-of-plane) and (k) and (l) ZX; The fracture locations are marked with red arrows. (For interpretation of the references to colour in this figure legend, the reader is referred to the Web version of this article.)

Table 5

Values of Poisson's ratio for specimens printed at different orientations.

Specimen orientation	Poisson's ratio
XY	0.311 ± 0.005
XY-45° (in plane)	0.305 ± 0.007
YX	0.310 ± 0.004
XZ	0.319 ± 0.002
XY-45° (out of plane)	0.333 ± 0.005
ZX	0.345 ± 0.004

close to the fractured cross section - points X_2 and Y_2. The mean values of the Vickers hardness, H_V, together with the standard deviation (STDEV) for each measurement are presented in Table 6. One can order the hardness data, measured before tensile test, from the highest to lowest with respect to the orientation during production, i.e.: XY, YX, XY-45° (in-plane), XZ, ZX and XY-45° (out-of-plane). This order is exactly the same as the one observed for UTS values reported earlier.

The hardness of all specimens after the tensile test, regardless of the printing strategy, are close the values within the range 113–118 kg/mm². A decrease in hardness of about 5–10 kg/mm² is observed for specimens XY, XY-45° (in-plane) and YX when compared to the hardness values measured before the tensile test. No considerable changes in hardness were found for the remaining specimens.

The relationship between hardness and strength of the material is explained in the next section.

3.2.1. Hardness-strength relationship

Table 7 shows a summary of linear strength-hardness relationship from literature for some metallic alloys with strain-hardening behaviour the same as Eq. (2).

Linear relationships between Vickers hardness H_{V5} (measured before tensile tests with a load of 5 kgf, presented in Table 6) versus yield stress and UTS (presented in Table 4) are observed as shown in Fig. 11(a) and (b), respectively. These linear correlations are as follows:

$$\sigma_y = 0.355 H_{V5} - 193.35 \tag{3}$$

$$UTS = 0.396 H_{V5} - 133.32 \tag{4}$$

The coefficients of determination, R^2, for Eqs. (3) and (4) are 0.97 and 0.90, respectively. It should be noted that the unit for σ_y, H_V and UTS is MPa. For material selection purposes for different applications, these linear relationships can be used as simple tool for converting hardness and UTS values to each other.

3.2.2. Hardness-equivalent strain relationship

Values of equivalent strain were calculated using Huber-von Mises-Hencky formula as follows [63–65]:

$$\varepsilon_e = \frac{1}{\sqrt{2}(1+v)}\left[\left(\varepsilon_x - \varepsilon_y\right)^2 + \left(\varepsilon_y - \varepsilon_z\right)^2 + \left(\varepsilon_z - \varepsilon_x\right)^2\right]^{1/2} \tag{5}$$

where ε_x, ε_y, ε_z are the principal strain components which are considered

Table 6

Vickers hardness of the specimens printed along different orientations.

Building direction	Before tensile test		After tensile test	
	H_V (kgf/mm²)	STDEV (kg/mm²)	H_V (kgf/mm²)	STDEV (kg/mm²)
XY	125.6	2.03	115.7	3.3
XY-45° (in-plane)	123.1	2.36	118.7	1.7
YX	125.2	3.65	114.5	0.5
XZ	116.9	1.20	113.8	2.4
XY-45° (out-of-plane)	110.9	1.25	112.1	3.0
ZX	113.0	4.50	112.8	0.5

Table 7

Details of linear strength-hardness equation for some metallic alloys with strain-hardening behaviour.

Material	Manufacturing method	Strength-hardness equation[a]	R^{2}[b]	Vickers hardness load (kgf)	Refs.
Aluminium alloy 7010	Traditional	$\sigma_y = 0.383 H_{V5} - 182.3$	0.957	5	[27, 30, 60, 61]
Al-0.4Si-0.50 Mg	LPBF	$\sigma_y = 0.383 H_{V2} - 101$	0.927	2	[62]
AlSi10Mg alloy	LPBF	$\sigma_y = 0.259 H_{V0.5} - 49.62$	0.86	0.5	[33]
AlSi10Mg alloy	LPBF	$UTS = 0.326 H_{V0.5} + 8.58$	–	0.5	[33]

[a] The unit for σ_y, H_V and UTS is MPa.
[b] Coefficients of determination.

here in the main axes x, y and z direction, respectively, and v is effective Poisson's ratio. For the uniaxial tensile loading, the strain along the z direction (perpendicular to the tensile loading direction, y) are the same as in direction x. Therefore, in this study, the strain component ε_z is assumed to be equal to ε_x measured in transvers direction using DIC system. So, Eq. (5) can be expressed in the following form:

$$\varepsilon_e = \frac{1}{\sqrt{2}(1+v)}\left[2\left(\varepsilon_x - \varepsilon_y\right)^2 + 4\varepsilon_x^2\right]^{1/2} \tag{6}$$

A relationship between hardness and equivalent strain in fracture regions can be another useful criterion to assess the mechanical behaviour of 3D printed aluminium alloys subjected to the tensile loading. In order to define the complex strain state in the fracture area, the DIC method is used which allows to capture the values of the strain components just before and after fracture. Applying the values of axial and transverse strain components and Poisson's ratio determined by DIC system to Eq. (6), one can calculate the equivalent strain, ε_e, for all specimens concerned. The values of both post tensile hardness and the equivalent strain strongly depend on the printing orientation of the AM specimens. A linear relationship between equivalent strain and post tensile Vickers hardness H_{V5} (presented in Table 6) is observed, as shown in Fig. 12, which is as follows:

$$\varepsilon_e = 0.00062 H_{V5} - 0.62 \tag{7}$$

The coefficients of determination, R^2, for Eq. (7) is 0.88. As it shows in Fig. 12, the values of both, the post tensile hardness and the equivalent strain strongly depend on the orientation of the specimens during AM process. The lowest value of equivalent strain and the corresponding post tensile hardness was observed for ZX specimen, while the highest for XY-45° (in-plane). The lowest and highest values of equivalent strain were 5% and 9%, for the ZX and XY, respectively. The highest changes in post tensile hardness were observed for the specimens printed in horizontal position (parallel to the build plate plane), namely XY, XY-45° (in-plane), YX. Their magnitudes are in the range 114–118 MPa, which is around 10 MPa less than that measured on the as-built material (before tensile test). This can be due to the higher sensitivity of hardness of these specimens to the axial strain under uniaxial tensile loading because as can be seen in Fig. 9(a), the axial strains before the fracture for the XY, XY-45° (in-plane) and YX specimens are higher than the other specimens. There were not significant difference between the values of hardness measured before and after the tensile test for the other three specimens, namely XZ, ZX and XY-45° (out-of-plane).

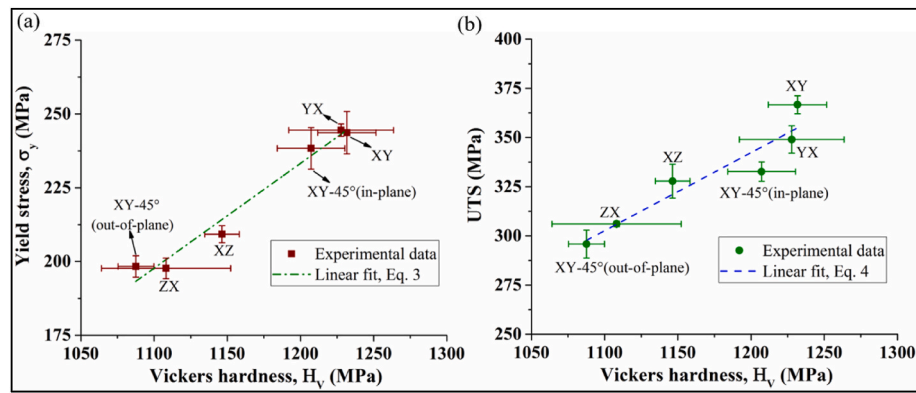Equation (7) can be used for the purpose of health monitoring of AM

Fig. 11. Linear correlation between Vickers hardness (measured before tensile tests) and (a) yield stress and (b) UTS measurements.
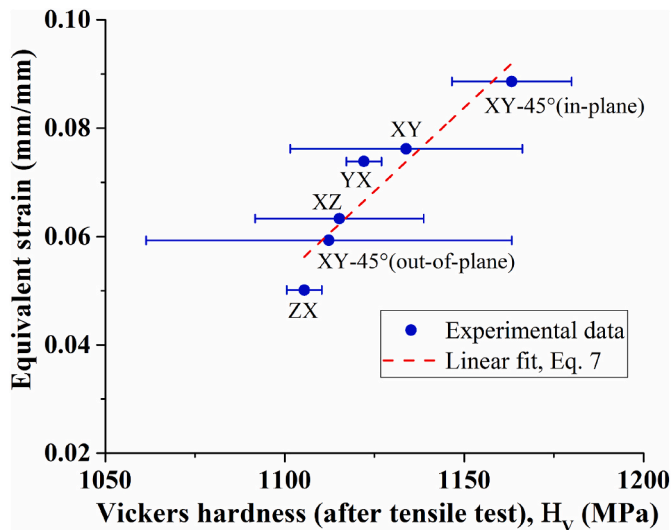

Fig. 12. Equivalent strain versus Vickers hardness (HV) measured after tensile test.

specimens under tensile loading. One can find equivalent strain of specimen using DIC, and then, use Eq. (7) to estimate post tensile hardness value (after fracture). After knowing post failure tensile value of the specimen/component and comparing it with the hardness before loading (as-built material), depending on the manufacturing orientation of the specimen/component, one can prevent failure of the specimen if the pre- and post tensile hardness values are close to each other.

3.3. Tensile fracture

Figs. 13–16 show selected SEM images of fractured surfaces of the specimens subjected to the tensile loading. Fig. 13(a) shows general view of cross-section of fractured surface of a XY specimen. Lack of fusion and pores are shown in Fig. 13(b)–(c), while the combination of even and uneven regions and slit-shape defects in Fig. 13(d). Fig. 14(a) shows cross-section view of fractured surface of a XZ specimen. Fig. 14 (b)–(d) depicts lack of fusion defect, cleavage surface and comparatively flat smooth surface after fracture, respectively. However, a magnified view of the flat cleavage surface indicates the presence of the individual protrusions on the fractured surface of the specimens analysed.

Fig. 15(a) shows networks of melt pool boundaries (distinguished by white arrows) along which fracture occurs for XY-45° (out-of-plane) specimens as it is evident in the magnified fracture surfaces in Fig. 15(c). Gas porosities and unmelted powders are shown in Fig. 15(b) and (d). The size of the unmelted powders matches those shown in Fig. 2. Fig. 16

(a) and (b) show full view of fractured surface and high magnification micrograph for dimple fracture for a ZX specimen, respectively. The dimples with the size of several micrometres, are indicative of coalescence of micro-voids.

4. Summary and conclusions

This research provided more insight on the effect of building orientation on the hardness and validity of strength-hardness relationships for AM materials. In this work, LPBF AlSi10Mg specimens were fabricated in six different orientations. XZ and YX showed lowest surface heights (R_a and R_z) while the other specimens showed similar surface roughness values. Significant strength and ductility variations were observed in the specimens. XY specimens showed the highest yield stress and ultimate tensile strength while XZ specimens exhibited the highest ductility. Hardness measurements before tensile tests for different specimens are in accordance with the tensile test results, following the same order as the UTS values: XY being the highest and XY-45° (out-of-plane) being the lowest. Linear relationships between experimental Vickers hardness (before tensile test) versus yield stress and UTS measurements are observed which can be used for converting hardness and yiled stress (or UTS) values to each other for material selection purposes and finding material properties for different applications. In turn, the values of hardness after the tensile test (post tensile hardness) measured in the fracture area of the specimens subjected to tensile loading were in the range 114–118 MPa for the specimens printed horizontally. Their hardness values for the specimens printed parallel to the build plate plane, namely XY, XY-45° (in-plane) and YX, decreased by amount of around 10 MPa. The change in hardness may be caused by different factors such as increase of microcracks developed around unmelted powders (fusion defects) and pores, during monotonic loading. Not a big difference between the values of hardness measured before and after the tensile test for the other three specimens, namely ZX and XY-45° (out-of-plane), were observed. The Huber-von Mises-Hencky equivalent strain values determined based on DIC observation in the fracture regions, as well yield stress and UTS measurement confirmed that the lowest values of hardness and post tensile hardness were obtained for the specimens printed in the vertical orientation, while the highest ones for the specimens printed in the horizontal orientation. The equivalent strain-hardness relationship can be used for health monitoring of AM specimens subject to tensile loading.

CRediT authorship contribution statement

A. Serjouei: Conceptualization, Methodology, Validation, Formal analysis, Visualization, Supervision, Writing – original draft. **T. Libura:** Investigation, Resources, Project administration, Writing – review & editing. **A. Brodecki:** Investigation, Resources, Data curation. **J. Radziejewska:** Investigation, Resources, Writing – review & editing. **P.**
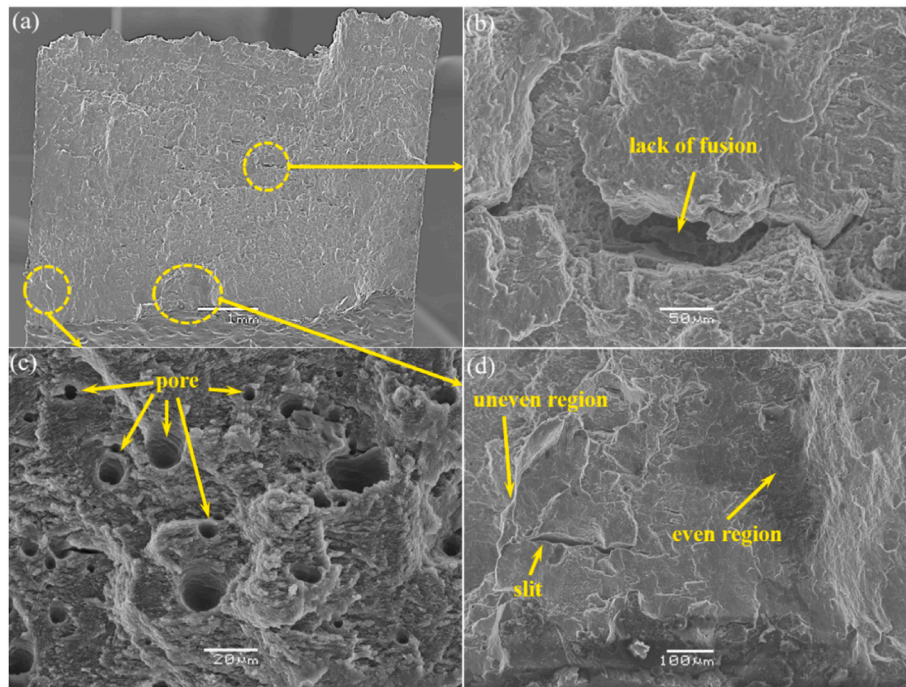
Fig. 13. SEM micrograph of fractured surface of XY specimen: (a) cross-section view; (b) lack of fusion defect; (c) pores and (d) slit shaped defect and even and uneven fractured regions.
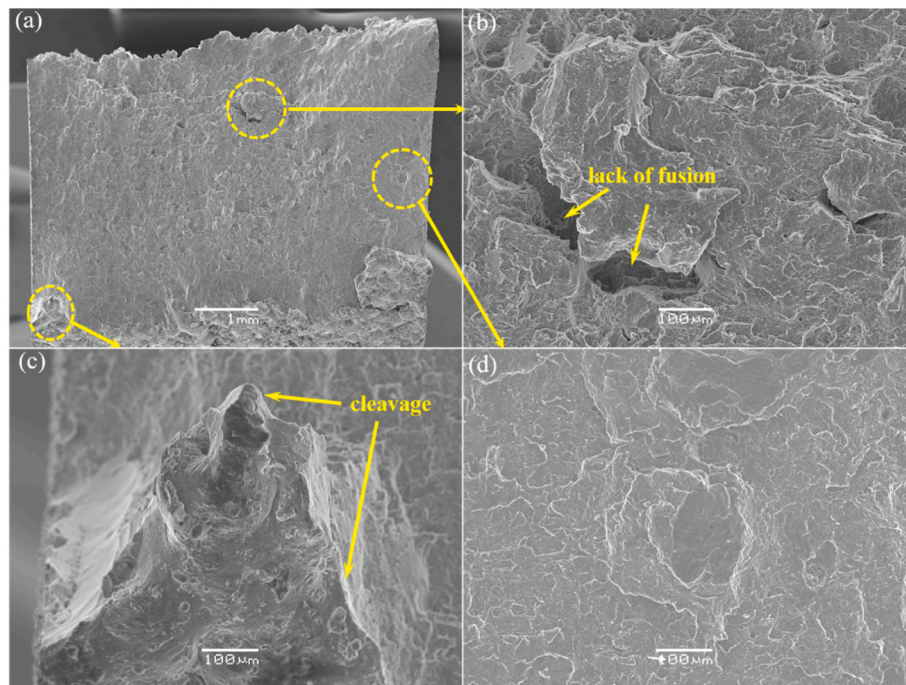

Fig. 14. SEM micrograph of fractured surface of XZ specimen: (a) cross-section view and (b) lack of fusion defect; (c) cleavage surface and (d) flat smooth surface after fracture.

Broniszewska: Investigation, Resources. **P. Pawłowski:** Investigation, Resources. **T. Szymczak:** Investigation, Writing – review & editing. **M. Bodaghi:** Investigation, Methodology, Writing - review & editing. **Z.L. Kowalewski:** Supervision, Project administration, Funding acquisition, Writing – review & editing.

Declaration of competing interest

The authors declare that they have no known competing financial interests or personal relationships that could have appeared to influence the work reported in this paper.
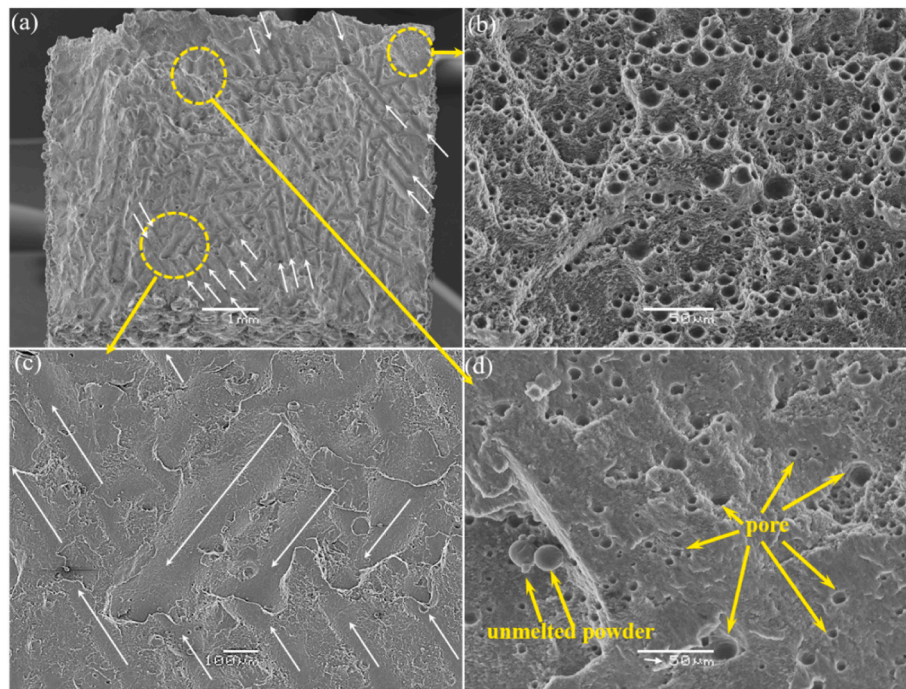
Fig. 15. SEM micrograph of fractured surface of XY-45° (out-of-plane) specimen: (a) cross-section view; (b) magnified view of gas porosities; (c) magnified melt pool tracks and (d) magnified view of section with unmelted powder and pores. White arrows in (a) and (c) show the parallel line scans or melt pools.
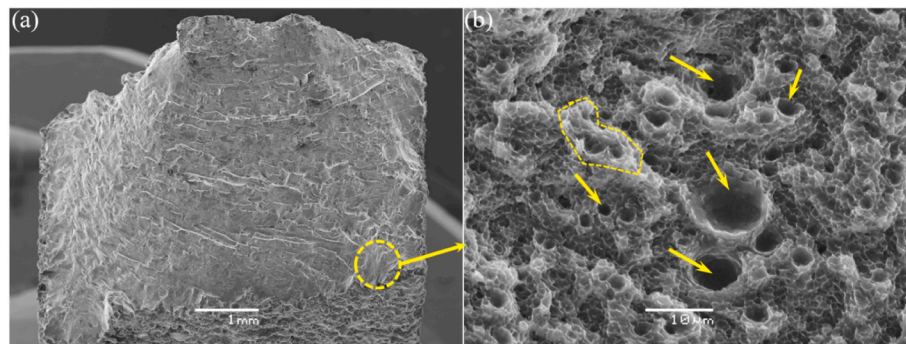

Fig. 16. SEM micrograph of fractured surface of a ZX specimen: (a) cross-section view and (b) dimple fracture; arrows show the dimples, and the dashed line shows coalescence of fine micro-size dimples.

Data availability

Data will be made available on request.

References

[1] P. Wood, T. Libura, Z.L. Kowalewski, G. Williams, A. Serjouei, Influences of horizontal and vertical build orientations and post-fabrication processes on the fatigue behavior of stainless steel 316L produced by selective laser melting, Materials 12 (24) (2019) 4203, https://doi.org/10.3390/ma12244203.

[2] A.M. Grbović, B.P. Rašuo, Nenad D. Vidanović, Mirjana M. Perić, Simulation of crack propagation in titanium mini dental implants (MDI), FME Trans 39 (4) (2011) 165–170.

[3] Gordana Kastratović, Nenad Vidanović, Aleksandar Grbović, Boško Rašuo, Approximate determination of stress intensity factor for multiple surface cracks, FME Trans 46 (1) (2018) 39–45.

[4] A. Grbovic, B. Rasuo, FEM based fatigue crack growth predictions for spar of light aircraft under variable amplitude loading, Eng. Fail. Anal. 26 (2012) 50–64, https://doi.org/10.1016/j.engfailanal.2012.07.003.

[5] A. Grbovic, B. Rasuo, Use of modern numerical methods for fatigue life predictions, in: Ricardo Branco (Ed.), Recent Trends in Fatigue Design, Series: Mechanical Engineering Theory and Applications, Nova Science Publishers, New York, 2015, pp. 31–74.

[6] J.H. Martin, B.D. Yahata, J.M. Hundley, J.A. Mayer, T.A. Schaedler, T.M. Pollock, 3D printing of high-strength aluminium alloys, Nature 549 (2017) 365.

[7] V. Petrovic, J. Vicente Haro Gonzalez, O. Jordá Ferrando, J. Delgado Gordillo, J. Ramón Blasco Puchades, L. Portolés Griñan, Additive layered manufacturing: sectors of industrial application shown through case studies, Int. J. Prod. Res. 49 (4) (2011) 1061–1079, https://doi.org/10.1080/00207540903479786.

[8] B. Amir, S. Samuha, O. Sadot, Influence of selective laser melting machine source on the dynamic properties of AlSi10Mg alloy, Materials (2019), https://doi.org/10.3390/ma12071143.

[9] S. Romano, A. Abel, J. Gumpinger, A.D. Brandão, S. Beretta, Quality control of AlSi10Mg produced by SLM: metallography versus CT scans for critical defect size assessment, Addit. Manuf. 28 (2019) 394–405, https://doi.org/10.1016/j.addma.2019.05.017.

[10] E. Brandl, U. Heckenberger, V. Holzinger, D. Buchbinder, Additive manufactured AlSi10Mg samples using selective laser melting (SLM): microstructure, high cycle fatigue, and fracture behavior, Mater. Des. 34 (2012) 159–169, https://doi.org/10.1016/j.matdes.2011.07.067.

[11] M. Muhammad, P.D. Nezhadfar, S. Thompson, A. Saharan, N. Phan, N. Shamsaei, A comparative investigation on the microstructure and mechanical properties of additively manufactured aluminum alloys, Int. J. Fatig. (2021), 106165, https://doi.org/10.1016/j.ijfatigue.2021.106165.

[12] N.T. Aboulkhair, N.M. Everitt, I. Ashcroft, C. Tuck, Reducing porosity in AlSi10Mg parts processed by selective laser melting, Addit. Manuf. 1–4 (2014) 77–86, https://doi.org/10.1016/j.addma.2014.08.001.

[13] A. Pola, D. Battini, M. Tocci, A. Avanzini, L. Girelli, C. Petrogalli, M. Gelfi, Evaluation on the fatigue behavior of sand-blasted AlSi10Mg obtained by DMLS, Frat. Ed. Integrità Strutt. 13 (49 SE-) (2019) 775–790, https://doi.org/10.3221/IGF-ESIS.49.69.

[14] L. Thijs, K. Kempen, J.-P. Kruth, J. Van Humbeeck, Fine-structured aluminium products with controllable texture by selective laser melting of pre-alloyed AlSi10Mg powder, Acta Mater. 61 (5) (2013) 1809–1819, https://doi.org/10.1016/j.actamat.2012.11.052.

[15] N. Read, W. Wang, K. Essa, M.M. Attallah, Selective laser melting of AlSi10Mg alloy: process optimisation and mechanical properties development, Mater. Des. 65 (2015) 417–424, https://doi.org/10.1016/j.matdes.2014.09.044.

[16] W. Li, S. Li, J. Liu, A. Zhang, Y. Zhou, Q. Wei, C. Yan, Y. Shi, Effect of heat treatment on AlSi10Mg alloy fabricated by selective laser melting: microstructure evolution, mechanical properties and fracture mechanism, Mater. Sci. Eng., A 663 (2016) 116–125, https://doi.org/10.1016/j.msea.2016.03.088.

[17] D. Manfredi, F. Calignano, M. Krishnan, R. Canali, E.P. Ambrosio, E. Atzeni, From powders to dense metal parts: characterization of a commercial AlSiMg alloy processed through direct metal laser sintering, Materials (2013), https://doi.org/10.3390/ma6030856.

[18] D. Manfredi, F. Calignano, M. Krishnan, R. Canali, E.P. Ambrosio, S. Biamino, D. Ugues, M. Pavese, F. Paolo, in: F. Calignano (Ed.), Additive Manufacturing of Al Alloys and Aluminium Matrix Composites (AMCs), IntechOpen, Rijeka, 2014, https://doi.org/10.5772/58534. Ch. 1.

[19] I. Yadroitsev, L. Thivillon, P. Bertrand, I. Smurov, Strategy of manufacturing components with designed internal structure by selective laser melting of metallic powder, Appl. Surf. Sci. 254 (4) (2007) 980–983, https://doi.org/10.1016/j.apsusc.2007.08.046.

[20] T. Kimura, T. Nakamoto, Microstructures and mechanical properties of A356 (AlSi7Mg0.3) aluminum alloy fabricated by selective laser melting, Mater. Des. 89 (2016) 1294–1301, https://doi.org/10.1016/j.matdes.2015.10.065.

[21] L. Thijs, F. Verhaeghe, T. Craeghs, J. Van Humbeeck, J.-P. Kruth, A study of the microstructural evolution during selective laser melting of Ti-6Al-4V, Acta Mater. 58 (9) (2010) 3303–3312, https://doi.org/10.1016/j.actamat.2010.02.004.

[22] B.J. Mfusi, L.C. Tshabalala, A.P.I. Popoola, N.R. Mathe, The effect of selective laser melting build orientation on the mechanical properties of AlSi10Mg parts, IOP Conf. Ser. Mater. Sci. Eng. 430 (2018), 12028, https://doi.org/10.1088/1757-899x/430/1/012028.

[23] K. Kempen, L. Thijs, J. Van Humbeeck, J.-P. Kruth, Mechanical properties of AlSi10Mg produced by selective laser melting, Phys. Procedia 39 (2012) 439–446, https://doi.org/10.1016/j.phpro.2012.10.059.

[24] F. Khodabakhshi, M. Haghshenas, H. Eskandari, B. Koohbor, Hardness-strength relationships in fine and ultra-fine grained metals processed through constrained groove pressing, Mater. Sci. Eng., A 636 (2015) 331–339, https://doi.org/10.1016/j.msea.2015.03.122.

[25] B. Chatterjee, P. Sahoo, Effect of strain hardening on elastic-plastic contact of a deformable sphere against a rigid flat under full stick contact condition, Adv. Tribol. 2012 (2012) 1–8, https://doi.org/10.1155/2012/472794.

[26] D. Tabor, The Hardness of Metals, Clarendon, Oxford, London, 1951.

[27] M. Tiryakioğlu, J.S. Robinson, M.A. Salazar-Guapuriche, Y.Y. Zhao, P.D. Eason, Hardness-strength relationships in the aluminum alloy 7010, Mater. Sci. Eng., A 631 (2015) 196–200, https://doi.org/10.1016/j.msea.2015.02.049.

[28] M.O. Lai, K.B. Lim, On the prediction of tensile properties from hardness tests, J. Mater. Sci. 26 (8) (1991) 2031–2036, https://doi.org/10.1007/BF00549163.

[29] C.H. Cáceres, J.R. Griffiths, A.R. Pakdel, C.J. Davidson, Microhardness mapping and the hardness-yield strength relationship in high-pressure diecast magnesium alloy AZ91, Mater. Sci. Eng., A 402 (1) (2005) 258–268, https://doi.org/10.1016/j.msea.2005.04.042.

[30] M.A. Salazar-Guapuriche, Y.Y. Zhao, A. Pitman, A. Greene, Correlation of strength with hardness and electrical conductivity for aluminium alloy 7010, Mater. Sci. Forum 519-521 (2006) 853–858. https://doi.org/10.4028/www.scientific.net/MSF.519-521.853.

[31] E.J. Pavlina, C.J. Van Tyne, Correlation of yield strength and tensile strength with hardness for steels, J. Mater. Eng. Perform. 17 (6) (2008) 888–893, https://doi.org/10.1007/s11665-008-9225-5.

[32] J.S. Keist, T.A. Palmer, Development of strength-hardness relationships in additively manufactured titanium alloys, Mater. Sci. Eng., A 693 (2017) 214–224, https://doi.org/10.1016/j.msea.2017.03.102.

[33] E. Cerri, E. Ghio, AlSi10Mg Alloy Produced by Selective Laser Melting: Relationships between Vickers Microhardness, Rockwell Hardness and Mechanical Properties, 2020.

[34] H. Nashid, C.G. Clifton, G. Ferguson, M. Hodgson, C.K. Seal, J.-H. Choi, Relationship between hardness and plastically deformed structural steel elements, Earthq. Struct. 8 (2015) 619–637.

[35] F.O. Sonmez, A. Demir, Analytical relations between hardness and strain for cold formed parts, J. Mater. Process. Technol. 186 (1) (2007) 163–173, https://doi.org/10.1016/j.jmatprotec.2006.12.031.

[36] A.E. Tekkaya, Improved relationship between Vickers hardness and yield stress for cold formed materials, Steel Res. 72 (8) (2001) 304–310, https://doi.org/10.1002/srin.200100122.

[37] M.M. Chaudhri, Subsurface strain distribution around Vickers hardness indentations in annealed polycrystalline copper, Acta Mater. 46 (9) (1998) 3047–3056, https://doi.org/10.1016/S1359-6454(98)00010-X.

[38] J. Lapin, M. Štamborská, K. Kamyshnykova, Experimental and numerical analysis of relations between Vickers hardness and plastic strain in nickel-based superalloy reinforced with carbide particles, SSRN Electron. J. (2022), https://doi.org/10.2139/ssrn.4069243.

[39] ASTM E8/E8M-09, Standard Test Methods for Tension Testing of Metallic Materials, ASTM International, West Conshohocken, PA, 2009.

[40] ISO 6507-1:2018 Metallic Materials — Vickers Hardness Test — Part 1: Test Method.

[41] EN ISO 6892-1:2016, Metallic Materials - Tensile Testing - Part 1 Method of Test at Room Temperature, International Organization for Standardization, 2016.

[42] S. Caba, Aluminum alloy for additive manufacturing in automotive production, ATZ Worldw 122 (11) (2020) 58–61, https://doi.org/10.1007/s38311-020-0285-y.

[43] P. Ponnusamy, R.A. Rahman Rashid, S.H. Masood, D. Ruan, S. Palanisamy, Mechanical properties of SLM-printed aluminium alloys: a review, Materials (2020), https://doi.org/10.3390/ma13194301.

[44] A. Hadadzadeh, B. Shalchi Amirkhiz, A. Odeshi, J. Li, M. Mohammadi, Role of hierarchical microstructure of additively manufactured AlSi10Mg on dynamic loading behavior, Addit. Manuf. 28 (2019) 1–13, https://doi.org/10.1016/j.addma.2019.04.012.

[45] A. Hadadzadeh, B.S. Amirkhiz, A. Odeshi, M. Mohammadi, Dynamic loading of direct metal laser sintered AlSi10Mg alloy: strengthening behavior in different building directions, Mater. Des. 159 (2018) 201–211, https://doi.org/10.1016/j.matdes.2018.08.045.

[46] C.h.S. Rakesh, N. Priyanka, R. Jayaganthan, N.J. Vasa, Effect of build atmosphere on the mechanical properties of AlSi10Mg produced by selective laser melting, Mater. Today Proc. 5 (9, Part 1) (2018) 17231–17238, https://doi.org/10.1016/j.matpr.2018.04.133.

[47] C.A. Biffi, J. Fiocchi, P. Bassani, A. Tuissi, Continuous wave vs pulsed wave laser emission in selective laser melting of AlSi10Mg parts with industrial optimized process parameters: microstructure and mechanical behaviour, Addit. Manuf. 24 (2018) 639–646, https://doi.org/10.1016/j.addma.2018.10.021.

[48] J. Bao, S. Wu, P.J. Withers, Z. Wu, F. Li, Y. Fu, W. Sun, Defect evolution during high temperature tension-tension fatigue of SLM AlSi10Mg alloy by synchrotron tomography, Mater. Sci. Eng., A 792 (2020), 139809, https://doi.org/10.1016/j.msea.2020.139809.

[49] N.T. Aboulkhair, I. Maskery, C. Tuck, I. Ashcroft, N.M. Everitt, Improving the fatigue behaviour of a selectively laser melted aluminium alloy: influence of heat treatment and surface quality, Mater. Des. 104 (2016) 174–182, https://doi.org/10.1016/j.matdes.2016.05.041.

[50] S.R. Ch, A. Raja, P. Nadig, R. Jayaganthan, N.J. Vasa, Influence of working environment and built orientation on the tensile properties of selective laser melted AlSi10Mg alloy, Mater. Sci. Eng., A 750 (2019) 141–151, https://doi.org/10.1016/j.msea.2019.01.103.

[51] J. Delahaye, J.T. Tchuindjang, J. Lecomte-Beckers, O. Rigo, A.M. Habraken, A. Mertens, Influence of Si precipitates on fracture mechanisms of AlSi10Mg parts processed by selective laser melting, Acta Mater. 175 (2019) 160–170, https://doi.org/10.1016/j.actamat.2019.06.013.

[52] A.A. Raus, M.S. Wahab, M. Ibrahim, K. Kamarudin, A. Ahmed, S. Shamsudin, Mechanical and physical properties of AlSi10Mg processed through selective laser melting, AIP Conf. Proc. 1831 (1) (2017), 20027, https://doi.org/10.1063/1.4981168.

[53] Y.J. Liu, Z. Liu, Y. Jiang, G.W. Wang, Y. Yang, L.C. Zhang, Gradient in microstructure and mechanical property of selective laser melted AlSi10Mg, J. Alloys Compd. 735 (2018) 1414–1421, https://doi.org/10.1016/j.jallcom.2017.11.020.

[54] D. Dai, D. Gu, M. Xia, C. Ma, H. Chen, T. Zhao, C. Hong, A. Gasser, R. Poprawe, Melt spreading behavior, microstructure evolution and wear resistance of selective laser melting additive manufactured AlN/AlSi10Mg nanocomposite, Surf. Coating. Technol. 349 (2018) 279–288, https://doi.org/10.1016/j.surfcoat.2018.05.072.

[55] L.F. Wang, J. Sun, X.L. Yu, Y. Shi, X.G. Zhu, L.Y. Cheng, H.H. Liang, B. Yan, L. J. Guo, Enhancement in mechanical properties of selectively laser-melted AlSi10Mg aluminum alloys by T6-like heat treatment, Mater. Sci. Eng., A 734 (2018) 299–310, https://doi.org/10.1016/j.msea.2018.07.103.

[56] L. Wang, J. Sun, X. Zhu, L. Cheng, Y. Shi, L. Guo, B. Yan, Effects of T2 heat treatment on microstructure and properties of the selective laser melted aluminum alloy samples, Materials (2018), https://doi.org/10.3390/ma11010066.

[57] EOS GmbH-Electro Optical Systems, Material data sheet EOS AlSi10Mg for EOSINT M280 400W & EOS M290 400W systems, munich, Germany, Accessed Date: https://fathommfg.com/wp-content/uploads/2020/11/EOS_Aluminium_AlSi10Mg_en.pdf. (Accessed 4 April 2021).

[58] J.R. Yates, P. Efthymiadis, A.A. Antonysamy, C. Pinna, J. Tong, Do additive manufactured parts deserve better? Fatig. Fract. Eng. Mater. Struct. 42 (9) (2019) 2146–2154, https://doi.org/10.1111/ffe.13092.

[59] B.C. Salzbrenner, J.M. Rodelas, J.D. Madison, B.H. Jared, L.P. Swiler, Y.-L. Shen, B. L. Boyce, High-throughput stochastic tensile performance of additively manufactured stainless steel, J. Mater. Process. Technol. 241 (2017) 1–12, https://doi.org/10.1016/j.jmatprotec.2016.10.023.

[60] M. Tiryakioğlu, J.S. Robinson, P.D. Eason, On the quench sensitivity of 7010 aluminum alloy forgings in the overaged condition, Mater. Sci. Eng., A 618 (2014) 22–28, https://doi.org/10.1016/j.msea.2014.09.002.

[61] R.J. Flynn, Property Prediction and Residual Stresses in Aluminium Alloy 7010, University of Limerick, Ireland, 2013.

[62] A.P. Sekhar, S. Nandy, K. Kumar Ray, D. Das, Hardness - yield strength relation of Al-Mg-Si alloys, IOP Conf. Ser. Mater. Sci. Eng. 338 (2018), 12011. 10.1088/1757-899x/338/1/012011.

[63] Z.L. Kowalewski, Assessment of cyclic properties of 18G2A low-alloy steel at biaxial stress state, Acta Mech. 120 (1) (1997) 71–89, https://doi.org/10.1007/BF01174317.

[64] Z.L. Kowalewski, M. Śliwowski, Effect of cyclic loading on the yield surface evolution of 18G2A low-alloy steel, Int. J. Mech. Sci. 39 (1) (1997) 51–68, https://doi.org/10.1016/0020-7403(96)00016-1.

[65] W. Szczepinski, On deformation-induced plastic anisotropy of sheet metals, Arch. Mech. 45 (1) (1993) 3–38.